

# Contents

<b>1</b>	<b>Theory</b>	<b>1</b>
1.1	Context . . . . .	1
1.2	Objective of this project . . . . .	2
1.3	The flow field equations . . . . .	3
1.4	The induced electric field equation . . . . .	3
1.5	Boundary conditions . . . . .	5
1.6	Skin effect . . . . .	6
<b>2</b>	<b>Numerical discretization</b>	<b>7</b>
2.1	Finite element method . . . . .	7
2.1.1	General considerations . . . . .	7
2.1.2	Galerkin finite element equations . . . . .	7
2.1.3	Elemental matrices for triangular elements . . . . .	9
2.1.4	Elemental matrices for edge elements . . . . .	10
2.1.5	Post-treatment of the solution . . . . .	10
<b>3</b>	<b>Numerical results</b>	<b>12</b>
3.1	Influence of the boundary condition set on the external domain . . . . .	12
3.2	Influence of the size of the external domain . . . . .	13
3.3	Convergence rate . . . . .	16
3.4	Influence of the electrical conductivity . . . . .	16
3.5	Influence of the excitation frequency . . . . .	17
3.6	Practical results . . . . .	19
3.6.1	VKI minitorch . . . . .	19
3.6.2	Tekna PL-50 model . . . . .	21
	<b>Bibliography</b>	<b>26</b>

# Chapter 1

## Theory

### 1.1 Context

When a shuttle or capsule enters the upper layers of a planetary atmosphere from space, it develops very high velocities. As denser, lower atmospheric layers are reached, the spacecraft loses its kinetic energy through collisions with molecules and atoms in the atmosphere. On a macroscopic scale, this gives rise to a strong, hypersonic bow shock in front of the vehicle. Behind the shock, density increases dramatically and temperatures rise to several thousands degrees K. To prevent damage to the spacecraft, its windward side needs to be protected by a heat shield, made of advanced thermal protection materials (TPMs). Because in-flight testing of new TPMs is prohibitively expensive, the aerospace community has developed high-temperature wind tunnels, in which samples of new TPMs may be tested prior to flight. In these wind tunnels, the extreme heat loads imposed on a thermal protection shield during hypersonic (re-)entry are reproduced by placing a sample of a TPM in a hot jet of thermal plasma.

Considerable interest has been devoted to applying inductively coupled radio frequency plasma (RF-ICP) in multi-material processing due to its higher temperature and plasma density, as well as the absence of contaminating electrodes. Hence, the ICP thermal plasma torch has rapidly replaced flames, direct current plasma, and other sources of ionization/excitation in various industrial fields, including semiconductor, biomedical, clinical, environmental, and geological or geochemical. The distinguishable performance of ICP compared to other plasma generation techniques have been widely required during the production of high purity materials, thin deposition, surface modification and waste treatment, and chemical synthesis and chemical processing. A commercially successful ICP technology requires the minimization of energy losses and the optimization of the process parameter affecting the plasma appearance and morphology. Indeed, the estimation of the plasma resistance and plasma impedance under different operating conditions is important to design a radio frequency (RF) generator. Moreover, a proper estimation of the plasma heated area must be determined to reduce the energy lost close to the side-wall. Therefore, to successfully implement an experimental RF- ICP system, it will be crucial to have a profound understanding of its basic functionality and control its discharge conditions in detail

A detailed photograph of a modern high-pressure ICP torch is shown in Fig. 1.1. A gas (air, argon, ...) is injected in a swirling, annular manner into a quartz tube, surrounded by a thick, water-cooled inductor. A powerful, radio-frequency electric current runs through the inductor and induces a secondary current through the gas inside the tube. Through Ohmic dissipation, the gas heats up to a partially ionized plasma with peak temperatures around 10.000 K. The swirling injection of gas close to the quartz tube stabilizes the plasma by promoting flow recirculation inside the torch; rather than sweeping away the discharge, the flow transports heat from the inductor zone back towards the inlet. Because of their high purity, high-pressure ICPs are the

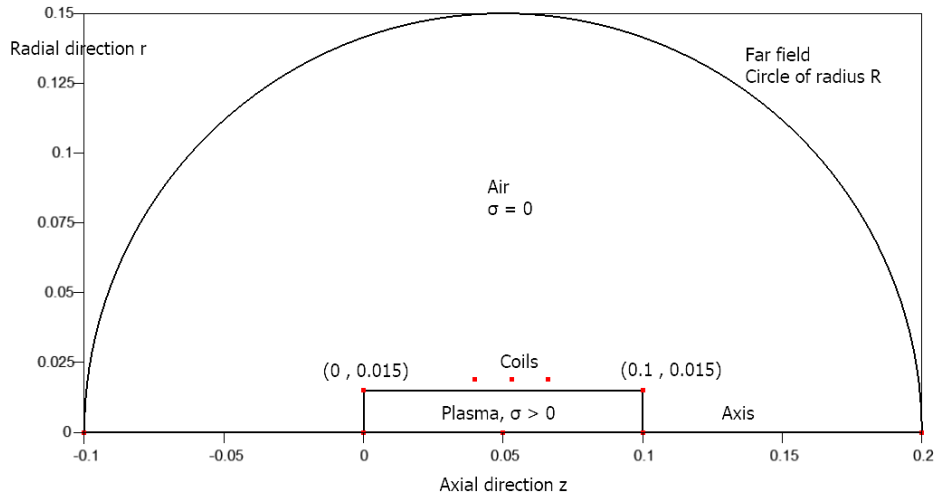
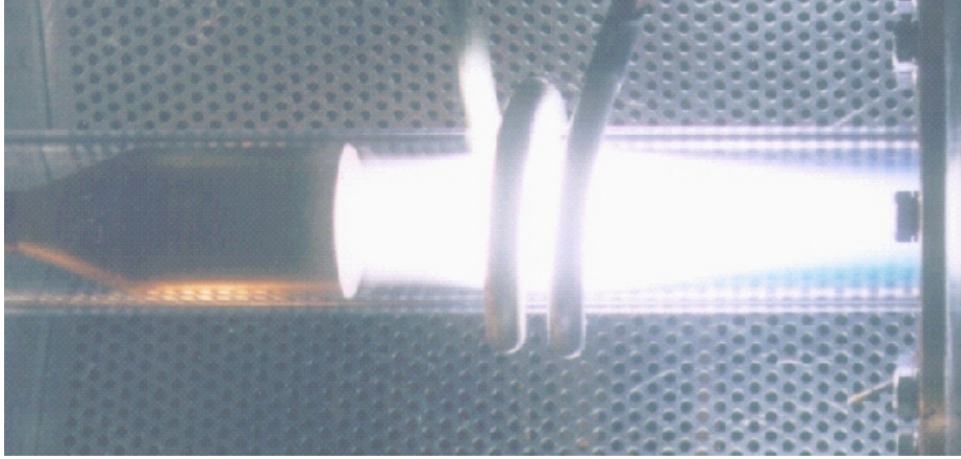


**Figure 1.1:** (top) VKI mini-torch in operation (0.1atm, 3kW, argon, 27MHz, photography from Vanden Abeele [1]). (bottom) Two-dimensional axisymmetric model of the inductively coupled plasma torch and its external domain.

preferred source of plasma in a wide variety of scientific and industrial applications, such as the deposition of metal coatings, the synthesis of ultra-fine powders and the generation of high purity silicon. High-pressure ICPs are close to local thermodynamic equilibrium and should not be confused with low-pressure inductive discharges, in which non-equilibrium processes play a dominant role. Operating at pressures of a few Pa or even less, low-pressure ICPs are used extensively in, for instance, the etching of semi-conductors.

## 1.2 Objective of this project

This project doesn't aim at solving the whole set of magnetohydrodynamics equations and physico-chemical transformations happening inside the plasma. This project will focus on the electrical part of the multiphysics modelling, covered later in Section 1.4. It will be supposed that the pressure are high so that the plasma is considered in local thermodynamic equilibrium (LTE), and the demixing of chemical elements can be neglected. So, the thermodynamic and transport properties can be expressed as a function of temperature and pressure only.

### 1.3 The flow field equations

Under the assumption of a steady flow, the Navier-Stokes equations take the following form

- Continuity equation

$$\nabla \cdot (\rho \mathbf{u}) = 0 \quad (1.1)$$

- Momentum equations

$$\rho \mathbf{u} \cdot \nabla \mathbf{u} = -\nabla p + \nabla \cdot (\mu \nabla \mathbf{u}) + \mathbf{F}_L \quad (1.2)$$

- Temperature equation

$$\rho C_p \mathbf{u} \cdot \nabla T = \nabla \cdot (\kappa \nabla T) + P_J \quad (1.3)$$

where  $\mathbf{u}[m/s]$  are the three-dimensional velocity components,  $\mu[kg/m.s]$ ,  $\rho[kg/m^3]$ ,  $C_p[J/kg.K]$  and  $\kappa[W/m.K]$  are the plasma dynamic viscosity, density, specific heat at constant pressure and thermal conductivity respectively. These equations are not solved in the present project but are merely mentioned in order to introduce the Lorentz force  $\mathbf{F}_L$  and the Joule heating rate  $P_J$ , which are the linking terms with the electromagnetic field.

### 1.4 The induced electric field equation

The electromagnetic field generated by the current density flowing through the coil,  $J_{coil}$ , and that induced in the plasma,  $J_{ind}$ , is governed by the Maxwell's equations

$$\nabla \cdot \mathbf{E} = \frac{\rho}{\epsilon_0} \quad (1.4a)$$

$$\nabla \cdot \mathbf{B} = 0 \quad (1.4b)$$

$$\nabla \times \mathbf{E} = -\frac{\partial \mathbf{B}}{\partial t} \quad (1.4c)$$

$$\nabla \times \mathbf{B} = \mu_0 (\mathbf{J}_{coil} + \mathbf{J}_{ind}) + \epsilon \mu_0 \frac{\partial \mathbf{E}}{\partial t} \quad (1.4d)$$

where  $\mathbf{E}$  and  $\mathbf{B}$  are the three-dimensional components of the electric and magnetic fields,  $\mu_0$  and  $\epsilon_0$  the permeability and permittivity of the free space and  $\rho$  the charge density. The charge density  $\rho$  is supposed null because the excitation frequency is by far smaller than the fundamental frequency of the plasma, which leads to a quasi-neutral state of the plasma. Furthermore the displacement current can also be neglected, which is done by splitting the electric field  $\mathbf{E}$  into the induced electric field  $\mathbf{E}_{ind}$  and the electric field generated by the coils  $\mathbf{E}_{coils}$ . The term  $\epsilon \mu_0 \partial \mathbf{E}_{ind} / \partial t$  is removed by neglecting the electromagnetic waves and the term  $\epsilon \mu_0 \partial \mathbf{E}_{coil} / \partial t$  is removed by neglecting the electric oscillations. The Maxwell's equations boil down to

$$\nabla \cdot \mathbf{E} = 0 \quad (1.5a)$$

$$\nabla \cdot \mathbf{B} = 0 \quad (1.5b)$$

$$\nabla \times \mathbf{E} = -\frac{\partial \mathbf{B}}{\partial t} \quad (1.5c)$$

$$\nabla \times \mathbf{B} = \mu_0 (\mathbf{J}_{coil} + \mathbf{J}_{ind}) \quad (1.5d)$$

It is convenient to introduce the magnetic vector potential  $\mathbf{A}$

$$\mathbf{B} = \nabla \times \mathbf{A} \quad (1.6)$$

which, introduced in the Maxwell's equations, lead to

$$\mathbf{E} = -\frac{\partial \mathbf{A}}{\partial t} \quad (1.7a)$$

$$\nabla^2 \mathbf{A} = -\mu_0 (\mathbf{J}_{coil} + \mathbf{J}_{ind}) \quad (1.7b)$$

The induced current density is expressed by the simplified Ohm's law

$$\mathbf{J}_{ind} = \sigma \mathbf{E} = -\sigma \frac{\partial \mathbf{A}}{\partial t} \quad (1.8)$$

Further simplifications are made by assuming a sinusoidal time variation with frequency  $f$ . The classical complex notation is then used to eliminate the time variable from Eq. (1.7b). To do so let us define

$$\mathbf{J}_{coil}(\mathbf{r}, t) = \Re \left\{ \tilde{\mathbf{J}}_{coil}(\mathbf{r}) e^{i\omega t} \right\} \quad (1.9a)$$

$$\mathbf{A}(\mathbf{r}, t) = \Re \left\{ \tilde{\mathbf{A}}(\mathbf{r}) e^{i\omega t} \right\} \quad (1.9b)$$

with  $\tilde{\mathbf{J}}_{coil}$  and  $\tilde{\mathbf{A}}$  the phasors and  $\omega = 2\pi f$ . One then gets

$$\nabla^2 \tilde{\mathbf{A}} - i\mu_0 \sigma \omega \tilde{\mathbf{A}} = -\mu_0 \tilde{\mathbf{J}}_{coil} \quad (1.10)$$

Under the assumption of an axisymmetric configuration for the induction circuit, the electric current density flowing in the coil and, consequently, the magnetic vector potential will only have tangential components. The electric current density  $\tilde{\mathbf{J}}_{coil}$  is purely real so that

$$\tilde{\mathbf{J}}_{coil} = J_{coil} \bar{\mathbf{e}}_\theta \quad (1.11a)$$

$$\tilde{\mathbf{A}} = (A_\theta^r + iA_\theta^i) \bar{\mathbf{e}}_\theta \quad (1.11b)$$

$$\tilde{\mathbf{E}} = (E_\theta^r + iE_\theta^i) \bar{\mathbf{e}}_\theta = \omega (A_\theta^i - iA_\theta^r) \bar{\mathbf{e}}_\theta \quad (1.11c)$$

Equation (1.10) can then be expressed in terms of electric field and be split into the followings

$$\frac{1}{r} \frac{\partial}{\partial r} \left( r \frac{\partial E_\theta^r}{\partial r} \right) + \frac{\partial^2 E_\theta^r}{\partial z^2} - \frac{E_\theta^r}{r^2} + \mu_0 \sigma \omega E_\theta^i = 0 \quad (1.12a)$$

$$\frac{1}{r} \frac{\partial}{\partial r} \left( r \frac{\partial E_\theta^i}{\partial r} \right) + \frac{\partial^2 E_\theta^i}{\partial z^2} - \frac{E_\theta^i}{r^2} - \mu_0 \sigma \omega E_\theta^r = \mu_0 \omega J_{coil} \quad (1.12b)$$

Provided that  $J_{coil}$  is known, equations (1.12a)-(1.12b) can be solved to calculate the induced electric field. The magnetic field can then be retrieved through Eq. (1.5c)

$$B_r = B_{zr} + iB_{zi} = \frac{1}{i\omega} \frac{\partial(E_\theta^r + iE_\theta^i)}{\partial z} = \frac{1}{\omega} \frac{\partial(E_\theta^i - iE_\theta^r)}{\partial z} \quad (1.13a)$$

$$B_z = B_{rr} + iB_{ri} = -\frac{1}{i\omega} \frac{1}{r} \frac{\partial r(E_\theta^r + iE_\theta^i)}{\partial r} = \frac{1}{\omega} \frac{1}{r} \frac{\partial r(-E_\theta^i + iE_\theta^r)}{\partial r} \quad (1.13b)$$

If an electric current  $I_{coil} = J_{coil} \Omega_{coil}$  flows through the coils of section  $\Omega_{coil}$ , then one can explicit the right-hand side of Eq. (1.12b). The outer inductor is approximated by a series of  $n_r$  parallel rings of radius  $R_i$  and axial position  $Z_i$

$$J_{coil}(z, r) = \sigma E_{coil}(z, r) = -i\omega \sigma A_{coil}(z, r) = -i\omega \sigma \frac{\mu_0 I_c}{2\pi} \sum_{i=1}^{n_r} \sqrt{\frac{R_i}{r}} G(m) \quad (1.14a)$$

$$G(m) = \frac{(2-m)K(m) - 2E(m)}{\sqrt{m}} \quad (1.14b)$$

$$m = \frac{4rR_i}{(r+R_i)^2 + (Z_i - z)^2} \quad (1.14c)$$

with  $K(m)$  and  $E(m)$  being the elliptic integrals of first and second kind, respectively.

The coupling with the fluid flow equations is done through the radial and axial components of the Lorentz force and through the Joule heating rate, see Section 1.3

$$F_r = \frac{\sigma}{2} \Re(E_\theta B_z^*) \quad (1.15a)$$

$$F_z = -\frac{\sigma}{2} \Re(E_\theta B_r^*) \quad (1.15b)$$

$$P_J = \frac{\sigma}{2} E_\theta E_\theta^* \quad (1.15c)$$

where the superscript  $*$  denotes the complex conjugate. The conversion efficiency can be retrieved by

$$\eta_c = \frac{P_{diss}}{P_{coil}} \quad (1.16)$$

with  $P_{diss}$  and  $P_{coil}$  are the RF dissipated power in the plasma and the power supplied to the coil respectively

$$P_{diss} = \int_V P_J dV \quad (1.17a)$$

$$P_{coil} = \frac{\pi f}{2\mu_0} \int_V (B_z^2 + B_r^2) dV \quad (1.17b)$$

## 1.5 Boundary conditions

The induced electric field must satisfy boundary conditions so that the system of equations built by the numerical method can be solved. On the axis, because of the axisymmetric hypothesis, the vanishing condition is imposed

$$E_\theta(z, 0) = 0 \quad (1.18)$$

Two approaches exist in terms of type of computational domain and associated boundary conditions. A first common configuration computes the electric field inside the torch only. This approach, introduced by McKelliget [2], solves the induction equations (1.12) inside the torch, each element inside the torch being considered as an infinitely thin current-carrying loop. The electric field on the boundary of the torch is obtained by summing up all the contributions coming from both excitation and induced currents flowing in the coil and in the plasma, respectively. Although mathematically elegant, this integral boundary procedure is computationally expensive, as it couples every boundary cell to all interior cells. Moreover, due to the term accounting for the effects of the induced currents, the whole distribution of  $E_\theta$  in the plasma region needs to be known to determine the vector potential at each point on the boundaries. Thus, an iterative approach has to be employed to solve the electromagnetic field equations, leading to slow convergence of the numerical process. This approach will not be implemented in this project.

Another approach uses a computational grid which extends well outside the plasma discharge region, so that simpler boundary conditions can be adopted for the electric field. Vanden Abeele [1] and Lopes [3] rely on a sufficiently large enough external domain to impose the vanishing conditions

$$E_\theta(z, r) = 0 \quad \text{if the external domain is large enough} \quad (1.19)$$

Bernardi *et al.* [4] introduced a new concept that allows the external domain to be considerably smaller without affecting the quality of the solution. The border of the external domain have been placed far enough from the plasma region in order to use boundary conditions for the electric field as if the torch were a magnetic dipole produced by the electric current flowing in the plasma and in the induction coil. Far enough away from the discharge, the whole system can be treated as a single magnetic dipole placed at the mid-coil point, with momentum parallel to the axis of the torch. Under such an assumption and taking a cylindrical  $(z, r)$  reference frame with the origin at the dipole and  $z$ -axis parallel to its momentum, the electric field at sufficient distance from the torch is given by the classic expression:

$$E_\theta(z, r) = C \frac{r}{(r^2 + z^2)^{(3/2)}} \quad (1.20)$$

In the later relation,  $C$  is a constant which accounts for the momentum of the dipole, whose value is not known *a priori* as it depends upon the induced currents which, in turn, depend upon the electric field in the discharge region. However, the value of  $C$  is not actually required for our purposes. By taking the  $z$ - and  $r$ -derivatives of Eq. (1.20) and eliminating the unknown constant  $C$ , one obtains boundary conditions to be applied on the external domain:

$$\frac{\partial E_\theta}{\partial z} = -\frac{3z}{r^2 + z^2} E_\theta \quad (1.21a)$$

$$\frac{\partial E_\theta}{\partial r} = \frac{1 - 3r^2(r^2 + z^2)^{-1}}{r} E_\theta \quad (1.21b)$$

## 1.6 Skin effect

According to Lenz's law, the currents in the plasma produce a magnetic field to counteract the electromagnetic field of the induction coil. This gives rise to a limitation of the penetration depth of the external magnetic field. This so-called skin-depth  $\delta$  depends on the electrical conductivity  $\sigma$  and the excitation frequency  $f$

$$\delta = \sqrt{\frac{1}{\pi f \mu_0 \sigma}} \quad (1.22)$$

The higher the electrical conductivity of the plasma and the higher the resonant frequency, the lower the skin-depth, and thus, the penetration of the external electromagnetic field into the plasma. This defines the tendency for alternating current (AC) signals to flow near the outer edge of the electrical conductor. The electric current takes the form

$$J(z, t) = J_0 e^{-z/\delta} \cos(\omega t - z/\delta) \quad (1.23)$$

with  $z$  the radial coordinate starting from the wall of the torch.

## Chapter 2

# Numerical discretization

### 2.1 Finite element method

#### 2.1.1 General considerations

The finite element (FE) method introduces the concept representation of the solution by functions. The spatial domain is discretized into elements of chosen shapes (triangles, quadrangles, etc.) and equations (1.12a) and (1.12b) are solved at the corners of these elements. The solution can be interpolated inside the elements through shape functions  $N_j(r, z)$ , for which the order will fix the precision of the result. The solution at any point in the two-dimensional space is then based on the knowledge of the solution  $E_j$  at the corners of the elements:

$$E(z, r) = \sum_k N_k(z, r) E_k \quad (2.1)$$

The numerical discretization of the physical equations does not allow the strict respect of the left-hand side being equal to the right-hand side. A residual is introduced in the physical equations. The FE method is based on the weighted minimalisation of the residual over the whole domain. In order to defined the discretized equation at node  $j$ , the Galerkin FE method picks the shape function at that node  $N_j(z, r)$  as the weight factor:

$$2\pi \int_{\Omega} r N_j(z, r) \left( \nabla^2 \tilde{\mathbf{E}}_j - i\mu_0 \sigma \omega \tilde{\mathbf{E}}_j - i\mu_0 \omega \tilde{\mathbf{J}}_{coilj} \right) dr dz = 0 \quad (2.2)$$

The shape functions are null everywhere except at the node  $j$  of interest. The choice of the Galerkin method has the consequence that only the direct neighbour nodes  $k$  are involved in the discretized equations at node  $j$ . These shape functions are moreover of order one because no special physical behaviour is expected.

#### 2.1.2 Galerkin finite element equations

Assuming an implicit summation over the index  $k$ , one can write down the Galerkin FE discretization of equations (1.12a) and (1.12b) at node  $j$  as

$$\int_{\Omega} r N_j \left( \frac{1}{r} \frac{\partial}{\partial r} \left( r \frac{\partial N_k}{\partial r} \right) E_{\theta k}^r + \frac{\partial^2 N_k}{\partial z^2} E_{\theta k}^r - \frac{N_k E_{\theta k}^r}{r^2} + \mu_0 \sigma \omega N_k E_{\theta k}^i \right) dr dz = 0 \quad (2.3a)$$

$$\int_{\Omega} r N_j \left( \frac{1}{r} \frac{\partial}{\partial r} \left( r \frac{\partial N_k}{\partial r} \right) E_{\theta k}^i + \frac{\partial^2 N_k}{\partial z^2} E_{\theta k}^i - \frac{N_k E_{\theta k}^i}{r^2} - \mu_0 \sigma \omega N_k E_{\theta k}^r - \mu_0 \omega J_{coil} \right) dr dz = 0 \quad (2.3b)$$



Integrating by part the two first terms of each equation allows the usage of shape functions of first order:

$$\int_{\Omega} \left( -r \frac{\partial N_j}{\partial r} \frac{\partial N_k}{\partial r} E_{\theta k}^r - r \frac{\partial N_j}{\partial z} \frac{\partial N_k}{\partial z} E_{\theta k}^r - \frac{N_j N_k E_{\theta k}^r}{r} + \mu_0 \sigma \omega r N_j N_k E_{\theta k}^i \right) dr dz + \underbrace{\int_{\partial\Omega} \left( r N_j n_r \frac{\partial E_{\theta}^r}{\partial r} + r N_j n_z \frac{\partial E_{\theta}^r}{\partial z} \right) d\Gamma}_{=\int_{\partial\Omega} r N_j \frac{\partial E_{\theta}^r}{\partial n} d\Gamma \text{ far field condition}} = 0 \quad (2.4a)$$

$$\int_{\Omega} \left( -r \frac{\partial N_j}{\partial r} \frac{\partial N_k}{\partial r} E_{\theta k}^i - r \frac{\partial N_j}{\partial z} \frac{\partial N_k}{\partial z} E_{\theta k}^i - \frac{N_j N_k E_{\theta k}^i}{r} - \mu_0 \sigma \omega r N_j N_k E_{\theta k}^r - \mu_0 \omega r N_j J_{coil} \right) dr dz + \underbrace{\int_{\partial\Omega} \left( r N_j n_r \frac{\partial E_{\theta}^i}{\partial r} + r N_j n_z \frac{\partial E_{\theta}^i}{\partial z} \right) d\Gamma}_{=\int_{\partial\Omega} r N_j \frac{\partial E_{\theta}^i}{\partial n} d\Gamma \text{ far field condition}} = 0 \quad (2.4b)$$

Note that the boundary integrals make appear the  $z$ - and  $r$ - derivatives of the electric field, which were specified in Eqs. (1.21). Taking into account that information, the boundary integral for the real component (and similarly for the imaginary one) becomes

$$\int_{\partial\Omega} r N_j \frac{\partial E_{\theta}^r}{\partial n} d\Gamma = \int_{\partial\Omega} N_j N_k \left( n_r \frac{(z - z_c)^2 - 2r^2}{r^2 + (z - z_c)^2} - 3n_z \frac{r(z - z_c)}{r^2 + (z - z_c)^2} \right) E_{\theta k}^r d\Gamma \quad (2.5)$$

where  $z_c$  is the axial location of the mid-coil point. For the sake of clarity, let us define the following elemental matrices

$$m_{jk} = \int_{\Omega} r N_j N_k dr dz \quad (2.6a)$$

$$k_{jk} = - \int_{\Omega} r \left( \frac{\partial N_j}{\partial r} \frac{\partial N_k}{\partial r} + \frac{\partial N_j}{\partial z} \frac{\partial N_k}{\partial z} \right) dr dz \quad (2.6b)$$

$$p_{jk} = - \int_{\Omega} \frac{N_j N_k}{r} dr dz \quad (2.6c)$$

$$s_{jk} = \int_{\partial\Omega} N_j N_k \left( n_r \frac{(z - z_c)^2 - 2r^2}{r^2 + (z - z_c)^2} - 3n_z \frac{r(z - z_c)}{r^2 + (z - z_c)^2} \right) d\Gamma \quad (2.6d)$$

These matrices are dependent on the shape functions only and can be evaluated through analytical expressions for some of them, or through numerical quadratures for others. Let us also use the same paradigm for the forcing term  $J_{coil}$  as for the unknown induced electric field:  $J_{coil}(z, r) = \sum_k N_k(z, r) J_{coil, k}$ . This allows the Galerkin FE to boil down to

$$(k_{jk} + p_{jk} + s_{jk}) E_{\theta k}^r + \mu_0 \omega \sigma_j m_{jk} E_{\theta k}^i = 0 \quad (2.7a)$$

$$(k_{jk} + p_{jk} + s_{jk}) E_{\theta k}^i - \mu_0 \omega \sigma_j m_{jk} E_{\theta k}^r = \mu_0 \omega m_{jk} J_{coil, k} \quad (2.7b)$$

or in terms of matrix representation

$$\begin{pmatrix} k_{jk} + p_{jk} + s_{jk} & \mu_0 \omega \sigma_j m_{jk} \\ -\mu_0 \omega \sigma_j m_{jk} & k_{jk} + p_{jk} + s_{jk} \end{pmatrix} \begin{pmatrix} E_{\theta k}^r \\ E_{\theta k}^i \end{pmatrix} = \begin{pmatrix} 0 \\ \mu_0 \omega m_{jk} J_{coil, k} \end{pmatrix} \quad (2.8)$$

The real and imaginary components are coupled through the term  $m_{jk}$ . In the case where the electrical conductivity  $\sigma$  of the medium is null, then only the imaginary component of the induced electric field is non-zero.

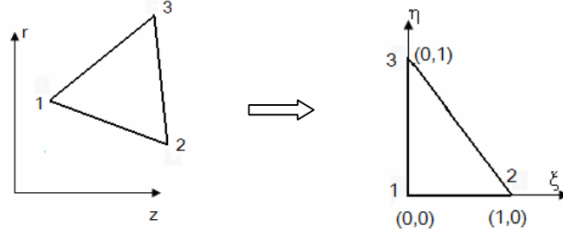


**Figure 2.1:** Definition of the triangular FE and its transformation to the  $(\xi, \eta)$  plane.

### 2.1.3 Elemental matrices for triangular elements

The analytical evaluation of the elemental matrices  $m_{jk}$  and  $k_{jk}$  is more easily performed in a new  $(\eta, \xi)$  plane defined in Fig. 2.1. Doing so the linear shape functions take the form

$$N_1(\eta, \xi) = 1 - \eta - \xi \quad (2.9a)$$

$$N_2(\eta, \xi) = \eta \quad (2.9b)$$

$$N_3(\eta, \xi) = \xi \quad (2.9c)$$

The integrals on this right triangle in  $(\xi, \eta)$  plane are related to the integrals on the true element (of area  $\Omega$ ) in the  $(z, r)$  plane by the Jacobian of the transformation which apply the element on the right triangle

$$\int_{\Omega} \psi(z, r) dr dz = \int_0^1 \int_0^{1-\xi} \psi(\eta, \xi) |J(\xi, \eta)| d\eta d\xi \quad (2.10)$$

where  $|J(\xi, \eta)|$  is the determinant of the Jacobian defined as

$$J(\eta, \xi) = \begin{pmatrix} \frac{\partial r}{\partial \xi} & \frac{\partial r}{\partial \eta} \\ \frac{\partial z}{\partial \xi} & \frac{\partial z}{\partial \eta} \end{pmatrix} \quad (2.11)$$

By choosing  $\psi = 1$  one gets the relation  $|J(\xi, \eta)| = 2\Omega$  which is easily computed. Let us define the normals of the segment on the other side of a node:

$$\mathbf{n}_1 = (r_3 - r_2)\bar{\mathbf{e}}_z + (z_2 - z_3)\bar{\mathbf{e}}_r \quad (2.12a)$$

$$\mathbf{n}_2 = (r_1 - r_3)\bar{\mathbf{e}}_z + (z_3 - z_1)\bar{\mathbf{e}}_r \quad (2.12b)$$

$$\mathbf{n}_3 = (r_2 - r_1)\bar{\mathbf{e}}_z + (z_1 - z_2)\bar{\mathbf{e}}_r \quad (2.12c)$$

Then the analytical expressions for the elemental matrices  $m_{jk}$  and  $k_{jk}$  are (see Detandt [5])

$$m_{jk} = \frac{\Omega(r_1 + r_2 + r_3 + r_j + r_k)(1 + \delta_{jk})}{60} \quad (2.13a)$$

$$k_{jk} = -\frac{(r_1 + r_2 + r_3)(n_j^r n_k^r + n_j^z n_k^z)}{12\Omega} \quad (2.13b)$$

The elemental matrix  $p_{jk}$  requires a numerical quadrature because of the difficulty to evaluate analytically. For this purpose, four internal quadrature points are taken in order to avoid any singularity at  $r = 0$  (see Table 2.1):

$$p_{jk} = -\int_{\Omega} \frac{N_j N_k}{r} dr dz = -\sum_{n=1}^4 w_n \frac{N_j(\eta_n, \xi_n) N_k(\eta_n, \xi_n)}{r_n} |J(\xi, \eta)| \quad (2.14)$$

n	$\xi$	$\eta$	$w$	$N_1$	$N_2$	$N_3$	r
1	1/3	1/3	-27/96	1/3	1/3	1/3	$(r_1 + r_2 + r_3)/3$
2	0.2	0.6	25/96	0.2	0.2	0.6	$0.2(r_1 + r_2) + 0.6r_3$
3	0.6	0.2	25/96	0.2	0.6	0.2	$0.2(r_1 + r_3) + 0.6r_2$
4	0.2	0.2	25/96	0.6	0.2	0.2	$0.2(r_2 + r_3) + 0.6r_1$

**Table 2.1:** Quadrature table for the element matrix  $p_{jk}$ .

d	$\xi$	$w$
1 and 2	$\pm 0.8611363116$	0.3478548451
3 and 4	$\pm 0.3399810436$	0.6521451548

**Table 2.2:** Quadrature table for the element matrix  $s_{jk}$ .

#### 2.1.4 Elemental matrices for edge elements

The boundary integral  $s_{jk}$  in Eq. (2.6) appears only on the nodes lying on the boundary of the external domain. The shape functions  $N_j$  and  $N_k$  are linear and  $(n_z, n_r)$  is the normal to the edge element, pointing outwards the domain. This elemental matrix is not simple and a numerical quadrature must be performed to compute it. To perform this numerical quadrature, the two nodes at  $(z_1, r_1)$  and  $(z_2, r_2)$  that define the edge element must be transformed to a new coordinate  $-1 \leq \xi \leq 1$  through the relation

$$z = z_1 + \frac{\xi + 1}{2}(z_2 - z_1) \quad (2.15a)$$

$$r = r_1 + \frac{\xi + 1}{2}(r_2 - r_1) \quad (2.15b)$$

The shape functions at the two nodes are then given by

$$N_1(\xi) = \frac{1 - \xi}{2} \quad (2.16a)$$

$$N_2(\xi) = \frac{1 + \xi}{2} \quad (2.16b)$$

and the quadrature is approximated by

$$s_{jk} = \sum_{d=1}^4 w_d N_j(\xi_d) N_k(\xi_d) \left( n_r \frac{(z_d - z_c)^2 - 2r_d^2}{r_d^2 + (z_d - z_c)^2} - 3n_z \frac{r(z_d - z_c)}{r_d^2 + (z_d - z_c)^2} \right) \frac{L}{2} \quad (2.17)$$

with  $L = \sqrt{(z_2 - z_1)^2 + (r_2 - r_1)^2}$  being the length of the edge element and the quadrature points  $\xi_d$  and weights  $w_d$  are defined in Table 2.2.

#### 2.1.5 Post-treatment of the solution

This section develops the expressions of the auxiliary data that results from the knowledge of the electric field. Let us start with the magnetic field, expressed by Eq. (1.13). Because the discretization has a linear interpolation inside the elements, the gradients of the electric field are constant inside the elements. This means that each node sees a different gradient inside each element it touches. In order to get a gradient at node  $i$ , the following average over the elements  $j$  is chosen:

$$\left. \frac{\partial E_i}{\partial n} \right|_{avg} = \frac{\sum_j \frac{\partial E_j}{\partial n} / \Omega_j}{\sum_j 1/\Omega_j} \quad (2.18)$$

The summation is performed over the elements  $j$  that touch node  $i$  and  $\Omega_j$  is the area of element  $j$ . This allows the smallest elements to have a more significant contribution and more precise values.

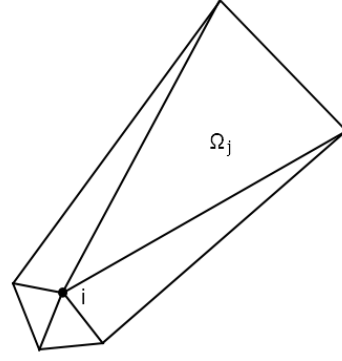


**Figure 2.2:** Average of the solution from the elements to the nodes.

In that last relation, the derivatives along the radial and axial directions inside each element  $j$  are given by

$$\frac{\partial E_j}{\partial r} = \sum_{k=1}^3 \frac{n_k^r}{2\Omega_j} E_{\theta k}, \quad \frac{\partial E_j}{\partial z} = \sum_{k=1}^3 \frac{n_k^z}{2\Omega_j} E_{\theta k} \quad (2.19)$$

The real and imaginary parts of the magnetic field at each node are then

$$\Re(B_r) = \frac{1}{\omega} \left. \frac{\partial E_{\theta}^i}{\partial z} \right|_{avg}, \quad \Im(B_r) = -\frac{1}{\omega} \left. \frac{\partial E_{\theta}^r}{\partial z} \right|_{avg}, \quad (2.20)$$

$$\Re(B_z) = -\frac{1}{\omega} \left( \frac{E_{\theta}^i}{r} + \left. \frac{\partial E_{\theta}^i}{\partial r} \right|_{avg} \right), \quad \Im(B_z) = \frac{1}{\omega} \left( \frac{E_{\theta}^r}{r} + \left. \frac{\partial E_{\theta}^r}{\partial r} \right|_{avg} \right) \quad (2.21)$$

## Chapter 3

# Numerical results

This chapter displays the results of the resolution of Equations (2.8) inside and around an inductively coupled plasma torch. The geometry of the whole domain and detail of the VKI minitorch are shown in Fig. 3.1. This minitorch has a diameter of  $3\text{cm}$ , an excitation frequency of  $27\text{MHz}$  and works with argon. The following sections will study

- the influence of the type of boundary condition set at the far field,
- the influence of the radius  $R$  of the external domain,
- the convergence rate of the numerical method as a function of degrees of freedom inside the torch,
- the influence of the electrical conductivity  $\sigma$  on the solution,
- the influence of the excitation frequency  $f$  of the coils

### 3.1 Influence of the boundary condition set on the external domain

This section studies the impact of the boundary condition set on the external domain. As explained in Section 1.5, two boundary conditions can be set, the vanishing one  $E_\theta = 0$  for

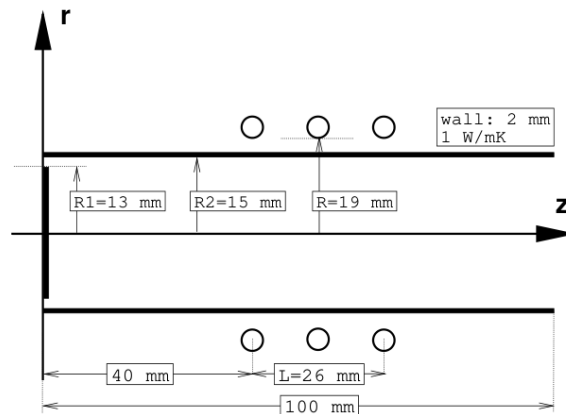


**Figure 3.1:** Geometry of the VKI minitorch (vanden Abeele [1]).

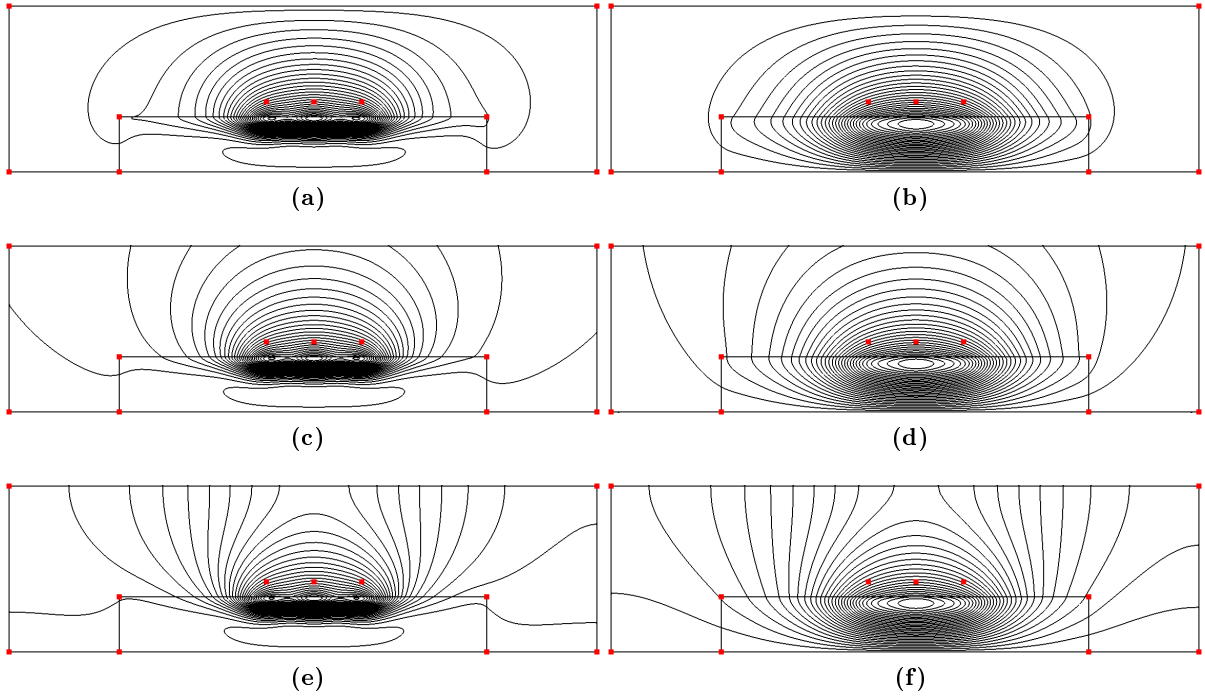


**Figure 3.2:** Influence of the boundary condition set on the external domain. Curves of isovalues of the (left) real part and (right) imaginary part of the induced electric field. (top)  $E_\theta = 0$ , (middle)  $\partial E_\theta / \partial n$  and (bottom)  $\partial E_\theta / \partial n = 0$  is set on the far field.

sufficiently large domains; and the specification of  $\partial E_\theta / \partial n$  for domains of smaller size. The outer domain consists here in a rectangle whose sides are offset by a distance  $R$  from each of the three sides of the torch. A large domain ( $R = 1m$ ) will be used as a reference for computations with a small external domain ( $R = 0.005m$ ). The additional boundary condition  $\partial E_\theta / \partial n = 0$  is also tested and is equivalent to cancelling the boundary integrals in Eqs (2.4).

Figures 3.2, 3.3 and 3.4 show the influence of the boundary condition set on the external domain on the induced electric field. Figure 3.2 shows curves of isovalues of the electric field when  $E_\theta = 0$ ,  $\partial E_\theta / \partial n$  or  $\partial E_\theta / \partial n = 0$  are imposed. In the case of  $E_\theta = 0$ , the forced containment of the electric field is clearly put forward. The case  $\partial E_\theta / \partial n = 0$  also fails to predict the correct electric field on the outer edge. Figures 3.3 and 3.4 show cuts along the radial and axial directions, at the middle coil  $z = 0.053m$  and on the wall of the torch  $z = 0.015m$  respectively. Only the imposition of  $\partial E_\theta / \partial n$  on the boundary leads to the best matching results in comparison with a large external domain. The condition  $E_\theta = 0$  displays non-physical behaviours at the left and right sides of the torch for  $\sigma \geq 1000S/m$ . The worst prediction with  $\partial E_\theta / \partial n$  is along the wall of the torch at low values of the electrical conductivity, for the imaginary part of  $E_\theta$ .

### 3.2 Influence of the size of the external domain

This section studies the impact of the size of the external domain. The outer domain consists here in a rectangle whose sides are offset by a distance  $R$  from each of the three sides of the torch. A large domain ( $R = 1m$ ) will be used as a reference, the distance being increased from  $R = 0.005m$  to  $1m$ . The additional boundary condition  $\partial E_\theta / \partial n = 0$  is also tested and is equivalent to cancelling the boundary integrals in Eqs (2.4). Three values of the electrical conductivity are taken ( $\sigma = 10^2, 10^3$  and  $10^4 S/m$ ) and the excitation frequency is set to 27MHz.

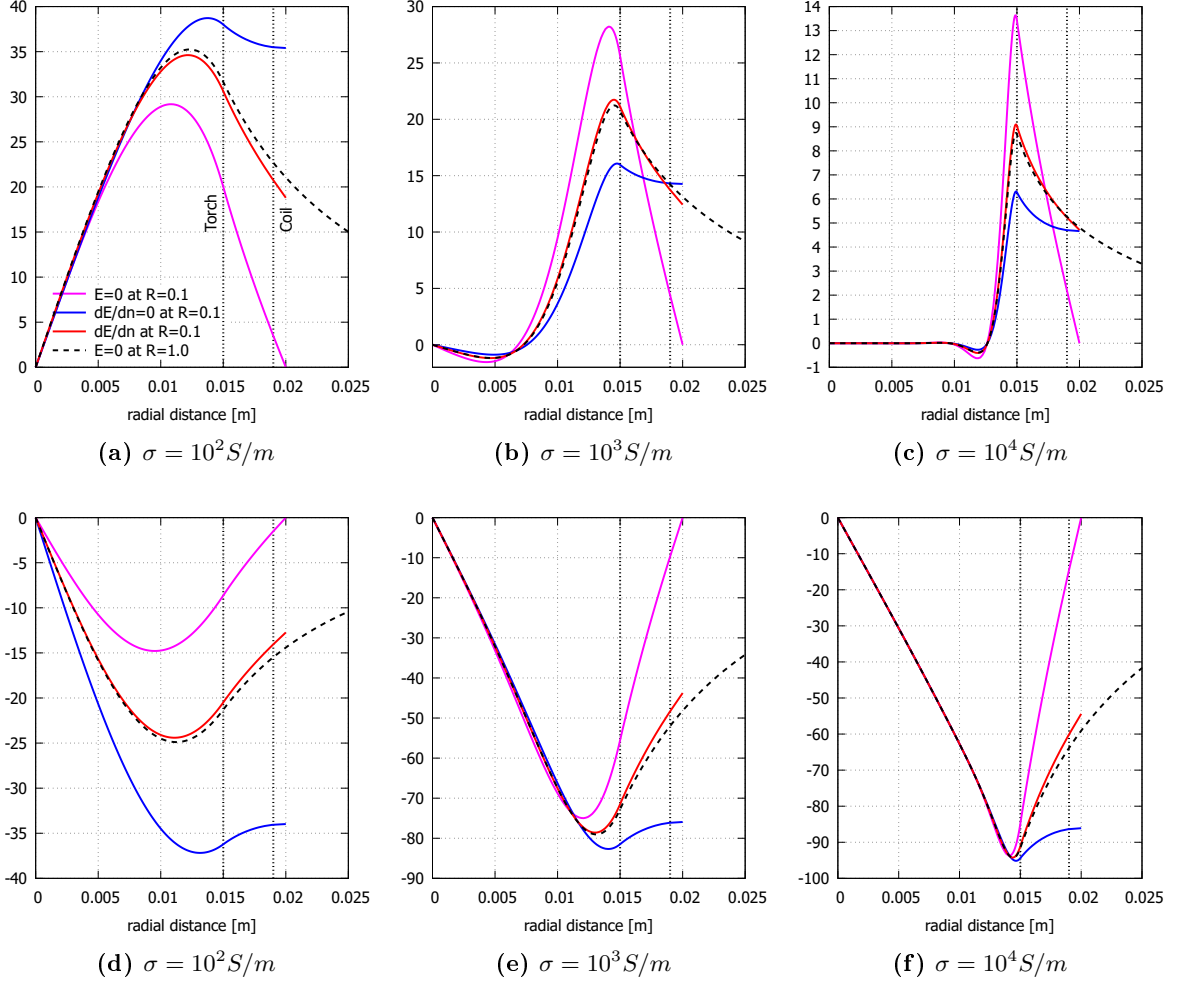


**Figure 3.3:** Influence of the boundary condition set on the external domain. Radial cut located at the middle coil ( $z = 0.053m$ ). (top) Real part and (bottom) imaginary part of the induced electric field for three values of the electrical conductivity  $\sigma$ .

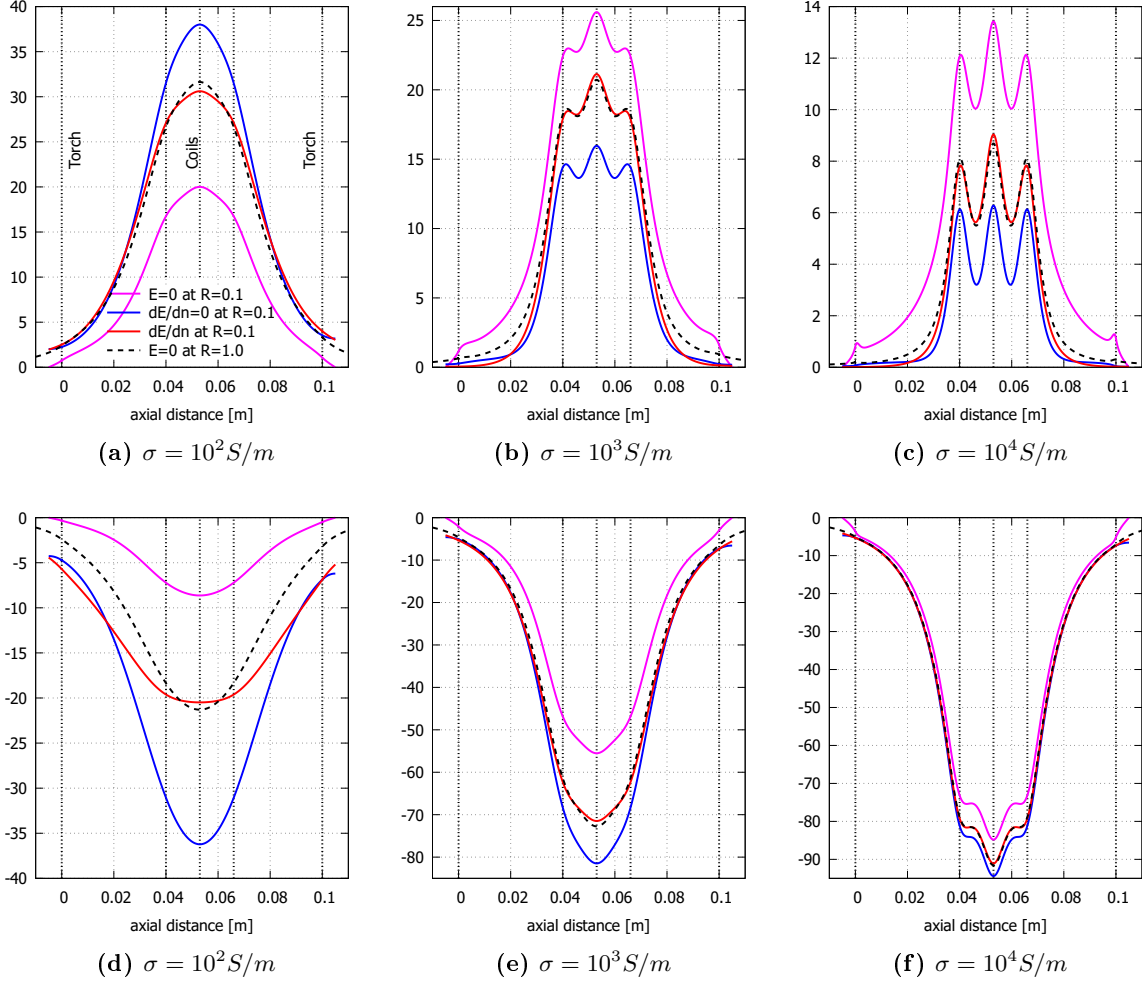


**Figure 3.4:** Influence of the boundary condition set on the external domain. Axial cut located on the torch ( $r = 0.015m$ ). (top) Real part and (bottom) imaginary part of the induced electric field for three values of the electrical conductivity  $\sigma$ .



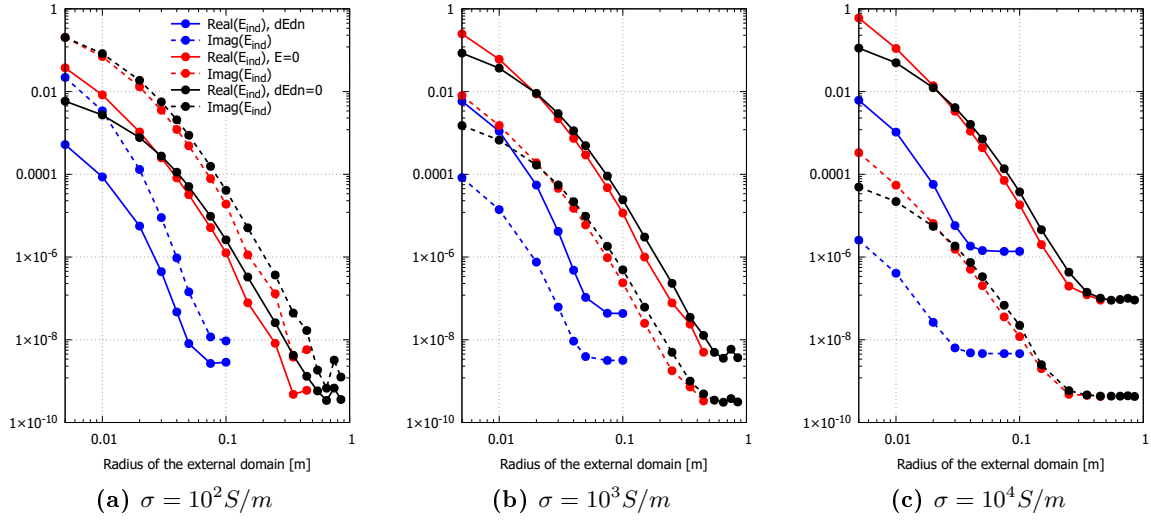


**Figure 3.5:** Influence of the size of the external domain on the solution. Relative error accumulated on the inside of the torch.

To measure the impact of the size of the external domain, the relative error for both real and imaginary parts of the electric field is defined as

$$\epsilon_{rel} = \sqrt{\frac{\sum_m (E_m - E_m^{R=1})^2}{\sum_m (E_m^{R=1})^2}} \quad (3.1)$$

where the index  $m$  runs for all the nodes inside the torch (and on its wall) and  $E^{R=1}$  is the reference solution computed with  $R = 1m$ . Figure 3.5 shows the relative error for the three boundary conditions at the outer edge, as a function of the distance  $R$ . Among all boundary conditions set on the external domain, the imposition of  $\partial E_\theta / \partial n$  displays the fastest convergence. It requires a distance  $R = 0.075m$  for  $\sigma = 10^2 S/m$  and a distance  $R = 0.04m$  for  $\sigma = 10^4 S/m$ . The two other boundary conditions require at least  $R = 0.4m$  before convergence. From now on it is supposed that the condition  $\partial E_\theta / \partial n$  is imposed on the outer edge as it displays the best behaviour.

### 3.3 Convergence rate

This section studies the convergence rate of the Galerkin finite element method by increasing the number of nodes inside the torch. The torch is meshed uniformly by right-angled triangles of identical leg size. The size of the external domain is chosen sufficiently big, see Section 3.2. The proof of convergence is based on the relative error from Eq. (3.1) where this time the reference field is the solution on the finest mesh. The results are shown in Fig. 3.6 for three values of the electrical conductivity. It appears that the Galerkin finite element method based on linear triangular elements has a convergence rate of  $-2$ .

### 3.4 Influence of the electrical conductivity

This section studies the impact of an increase in the electrical conductivity  $\sigma$  on the solution. The immediate impact of such an increase is the decrease of the skin-depth of the total electric field, as explained in Section 1.6. Figure 3.7 shows the real and imaginary parts of the induced and

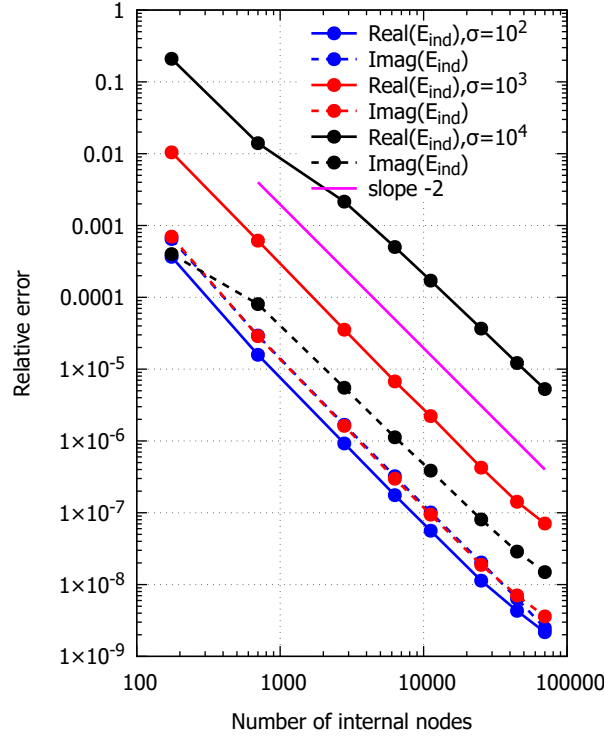


**Figure 3.6:** Convergence rate

$\sigma$	Theoretical $\delta$	Numerical $\delta$
$10^2 S/m$	$9.58mm$	$8.54mm$
$10^3 S/m$	$3.03mm$	$3.07mm$
$10^4 S/m$	$0.96mm$	$0.97mm$

**Table 3.1:** Theoretical and numerically computed skin-depths as a function of the electrical conductivity.

total electric fields as well as the purely imaginary contribution from the coils. The calculation of the skin-depth is based on the norm of the total electric field

$$\|E_{tot}\| = \sqrt{(E_{\theta}^r)^2 + (E_{\theta}^i + E_{coil})^2} \quad (3.2)$$

For an excitation frequency  $f = 27.6MHz$ , the theoretical skin-depth from Eq. (1.22) and the numerically computed ones are given in Table 3.1. A pretty good agreement emerges, especially for high values of  $\sigma$ .

### 3.5 Influence of the excitation frequency

This section studies the impact of an increase in the excitation frequency  $f$  on the solution. The immediate impact of such an increase is the decrease of the skin-depth of the total electric field, as explained in Section 1.6. Figure 3.7 shows the real and imaginary parts of the induced and total electric fields as well as the purely imaginary contribution from the coils. Note that contrary to the previous section, the amplitude of the forcing term is directly proportional to  $\omega$  (see Eq (1.14a)), which explains the linear variation of the amplitude of  $E_{coil}$  as  $f$  increases.

The calculation of the skin-depth is based on the norm of the total electric field

$$\|E_{tot}\| = \sqrt{(E_{\theta}^r)^2 + (E_{\theta}^i + E_{coil})^2} \quad (3.3)$$

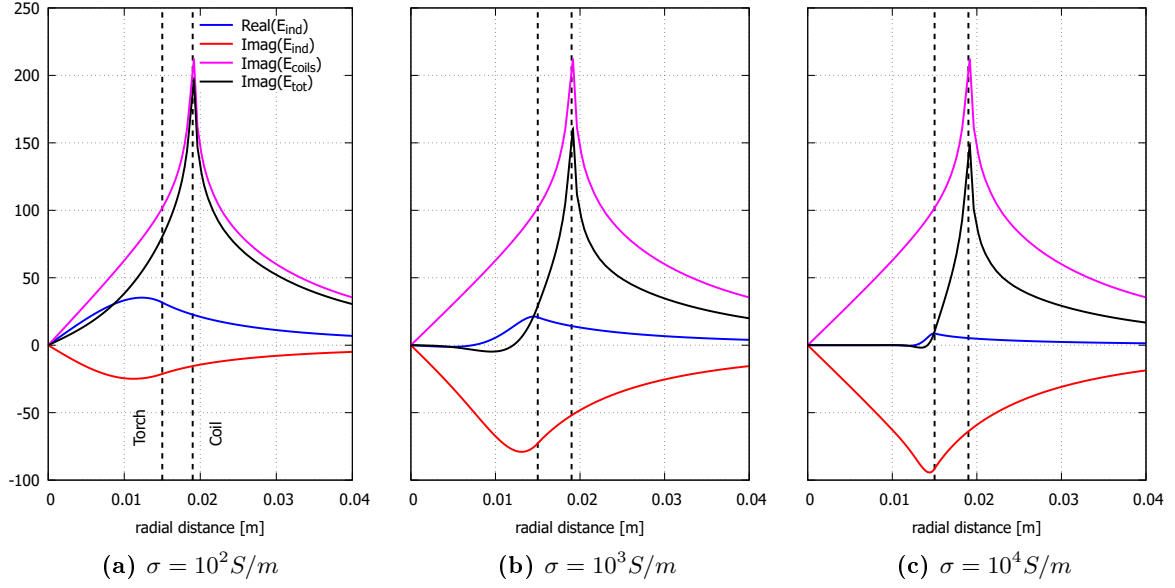


**Figure 3.7:** Influence of the electrical conductivity  $\sigma$  on the solution. Cut at  $z = 0.053m$  located at the middle coil.

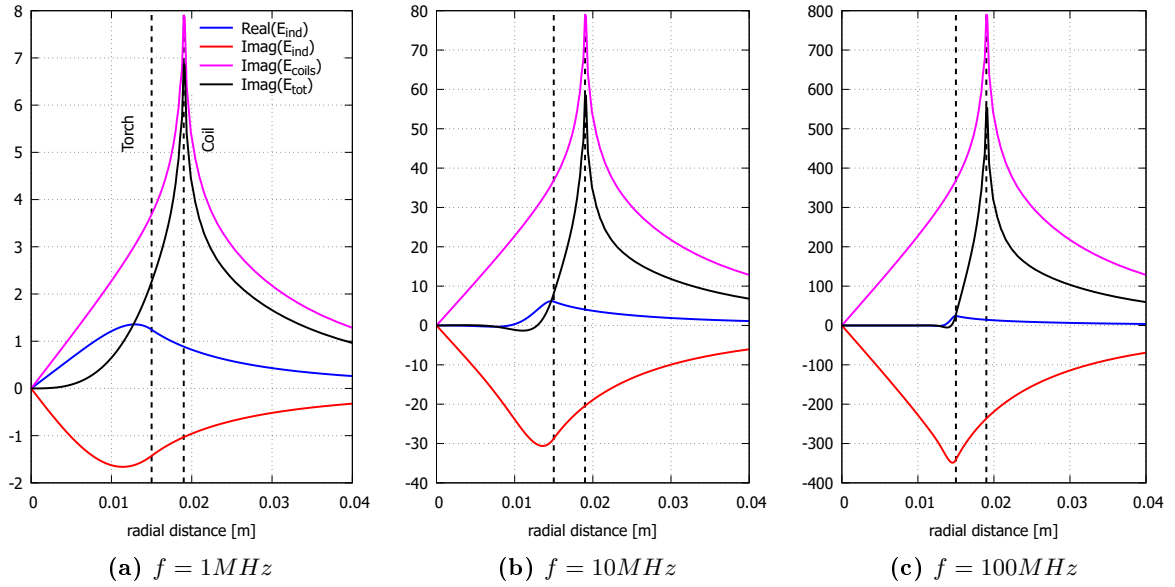


**Figure 3.8:** Influence of the excitation frequency  $f$  on the solution. Cut at  $z = 0.053m$  located at the middle coil.

$f$	Theoretical $\delta$	Numerical $\delta$
1MHz	7.12mm	7.79mm
10MHz	2.25mm	2.26mm
100MHz	0.71mm	0.72mm

**Table 3.2:** Theoretical and numerically computed skin-depths as a function of the excitation frequency.

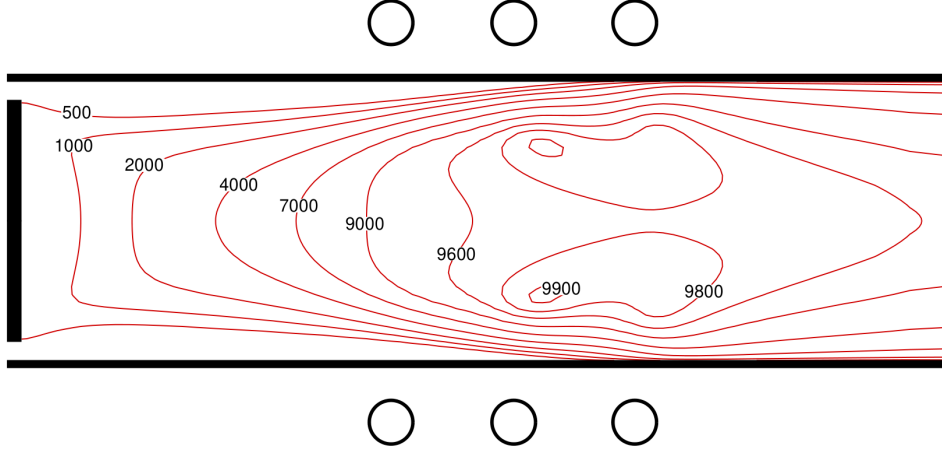


**Figure 3.9:** Distribution of temperature inside the VKI minitorch, figure from vanden Abeele ([1], Fig. 7.1).

For an electrical conductivity  $\sigma = 5000S/m$ , the theoretical skin-depth from Eq. (1.22) and the numerically computed ones are given in Table 3.2. A pretty good agreement emerges, especially for high values of  $f$ .

## 3.6 Practical results

This section illustrates the usage of the code on practical situations.

### 3.6.1 VKI minitorch

Let us consider the situation of the high-pressure VKI minitorch described in vanden Abeele [1]. The chosen plasma is argon under *Local Thermal Equilibrium* (LTE) condition. The operating pressure is 1atm, the excitation frequency  $f = 27MHz$  and the power 3kW.

The distribution of the temperature resulting from the interaction between the flow and the electromagnetic field has been computed by vanden Abeele [1] and is shown in Fig. 3.9. The electrical conductivity of the plasma can be estimated on the basis of the knowledge of the curve shown in Fig. 3.10 (from Lopes [3]). This electrical conductivity has been crudely extracted and is used as an input parameter to the computation (see distribution of  $\sigma$  in Fig. 3.11). The power specified was used to estimate the intensity of the electric current inside the coils (the power is proportional to  $I_c^2$ ,  $I_c = 49A$  here). Iterations on  $I_c$  were made in order to more or less match the values of the electric field surrounding the coils in comparison with the results from vanden Abeele [1]. The resulting total electric field is compared with the one from vanden Abeele [1] and displays a very good agreement. Because of the crude distribution of  $\sigma$  inside the torch and because  $\sigma$  is set to zero outside the torch (no information on the temperature distribution outside the torch is available), the curves are a little bit offset in the downstream part of the torch but that remains very localized.

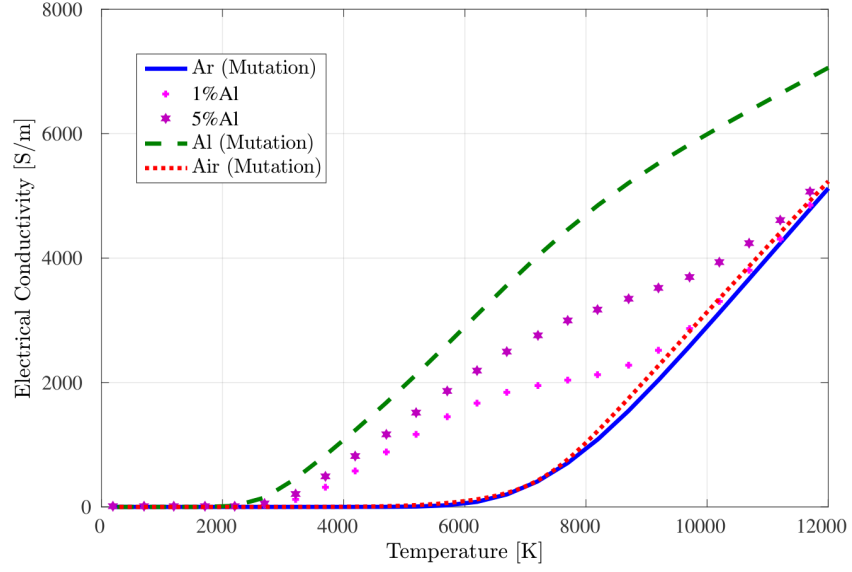


**Figure 3.10:** Electrical conductivity of argon as a function of temperature for constant pressure ( $1atm$ ). Figure from Lopes [3] (Fig. 2.5).

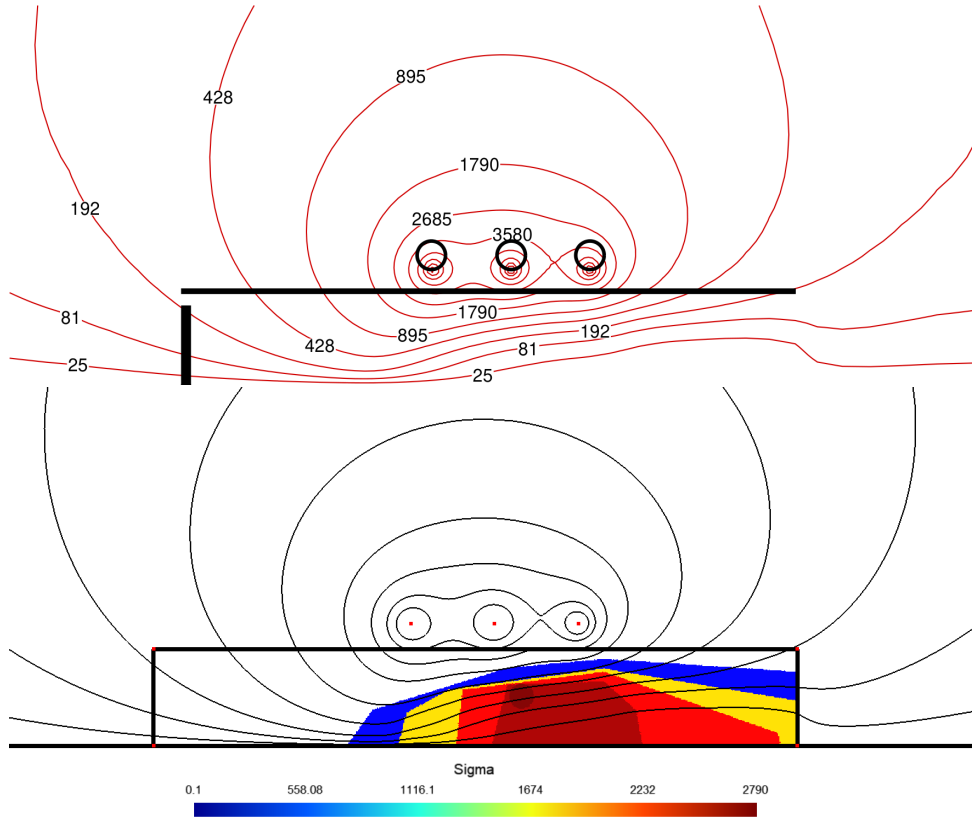


**Figure 3.11:** Iso-value lines of the norm of the electric field in the VKI minitorch. (top) results from vanden Abeele ([1], Fig. 7.1) and (bottom) present results with iso-contours of the electrical conductivity  $\sigma$ .

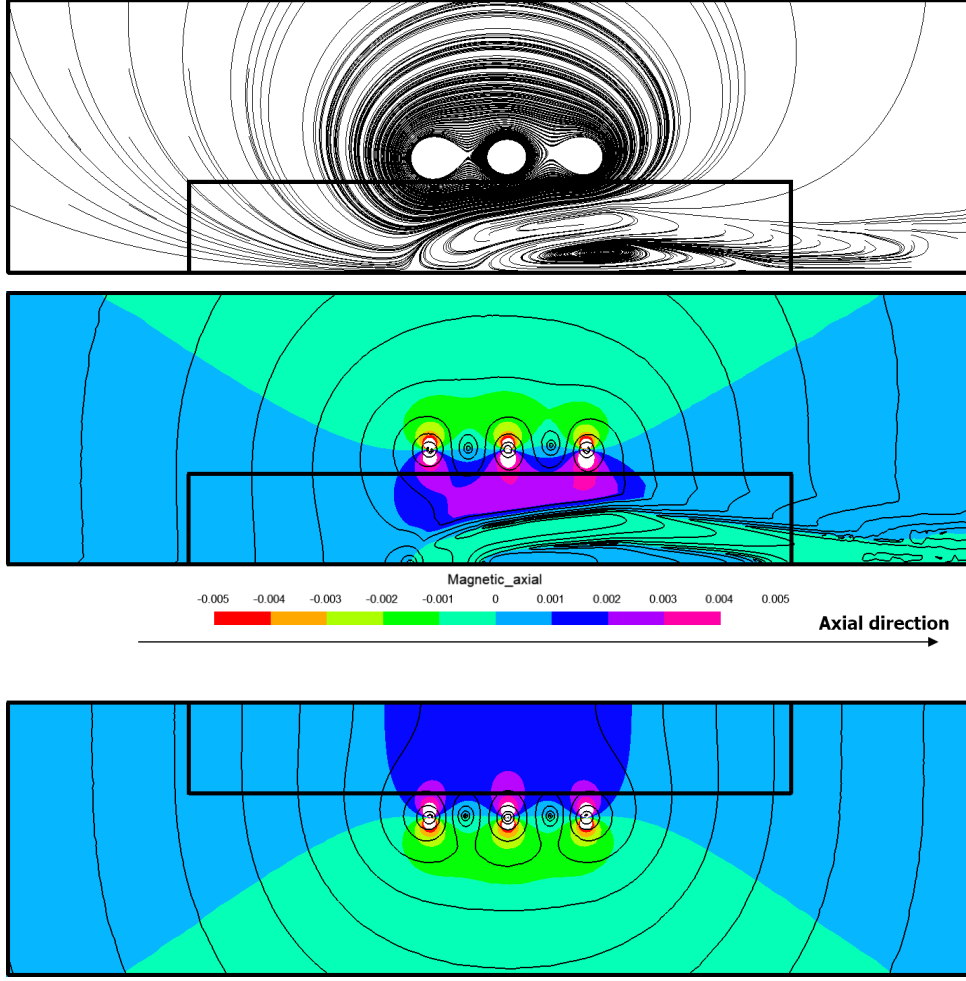
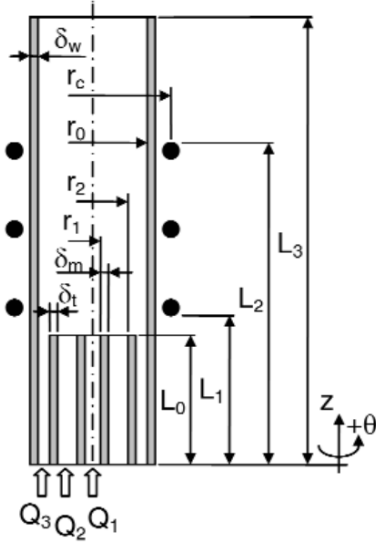


**Figure 3.12:** (top) Streamlines of the magnetic field. (middle and bottom) Iso-value lines of the norm of the magnetic field are superposed over the distribution of the axial component of the magnetic field. (middle) Present results with distribution of the electrical conductivity and (bottom) without plasma inside the torch.

Figure 3.12 shows three informations: streamlines of the magnetic field, iso-value lines of the norm of the magnetic field and the distribution of its axial component (in colour). The present results are compared with the situation where  $\sigma = 0$  is set inside the torch, which is equivalent to no plasma present. This comparison puts forwards the deformation of the magnetic field lines. Moreover it appears that a significant region inside the torch (and its downwards part) have a negative axial magnetic component of small amplitude. This indicates the presence of a double 'recirculating bubble' and pictured at the top of Fig. 3.12 .

### 3.6.2 Tekna PL-50 model

The same technique of reconstruction of the electrical conductivity is applied for the Tekna PL-50 model (Tekna Plasma Systems, Inc., see Fig. 3.13). The temperature field is extracted from Bernardi *et al.* [4] and the electrical conductivity can be reconstructed with the help of Fig. 3.10. The discharge is assumed to be operated in argon at atmospheric pressure. The net power dissipated in the plasma,  $P$ , is 5kW while the RF generator frequency,  $f$ , is set at 3 MHz. The coil current is set to 150A in order to sustain the 5kW plasma discharge, as reported by Bernardi *et al.* [4].



Dimensions and operating conditions	
$L_0 = 50 \text{ mm}$	$L_2 = 120 \text{ mm}$
$L_1 = 60 \text{ mm}$	$L_3 = 200 \text{ mm}$
$r_0 = 25 \text{ mm}$	$\delta_w = 3.5 \text{ mm}$
$r_1 = 1.5 \text{ mm}$	$\delta_m = 2.0 \text{ mm}$
$r_2 = 18.8 \text{ mm}$	$\delta_t = 2.2 \text{ mm}$
$r_c = 33 \text{ mm}$	$d_c = 6 \text{ mm}$
$Q_1 = 1 \text{ slpm}$	$Q_3 = 31 \text{ slpm}$
$Q_2 = 3 \text{ slpm}$	
$P = 5 \text{ kW}$	$f = 3 \text{ MHz}$

**Figure 3.13:** Geometry, dimensions and operating conditions of the Tekna PL-50, from Bernardi *et al.* [7].

The resulting complex electrical field is displayed in Figures. 3.14 and 3.15 along with the results from Bernardi *et al.* [6]. A very good agreement is met again. Figure 3.16 shows the electric field along axial and radial cuts alongside with numerical results from Bernardi *et al.* [6]. The results are encouragingly in good agreement with the reference if one considers the present crude approximation of the spatial distribution for the electrical conductivity.

Lines of iso-values of the norm of the magnetic field are displayed on Fig. 3.17 in parallel with the distribution of the axial component of the magnetic field. For comparison, results without plasma in the torch ( $\sigma = 0$  everywhere) are also displayed. It appears that a region of reverse axial magnetic field is present inside the torch. This indicates the presence of a single 'recirculating bubble' in the magnetic field, as shown at the top of Fig. 3.17, that extends a little bit outside of the torch. This is intrinsically linked with the region of negative values taken by the imaginary part of the total electric field, as displayed in Fig. 3.16.

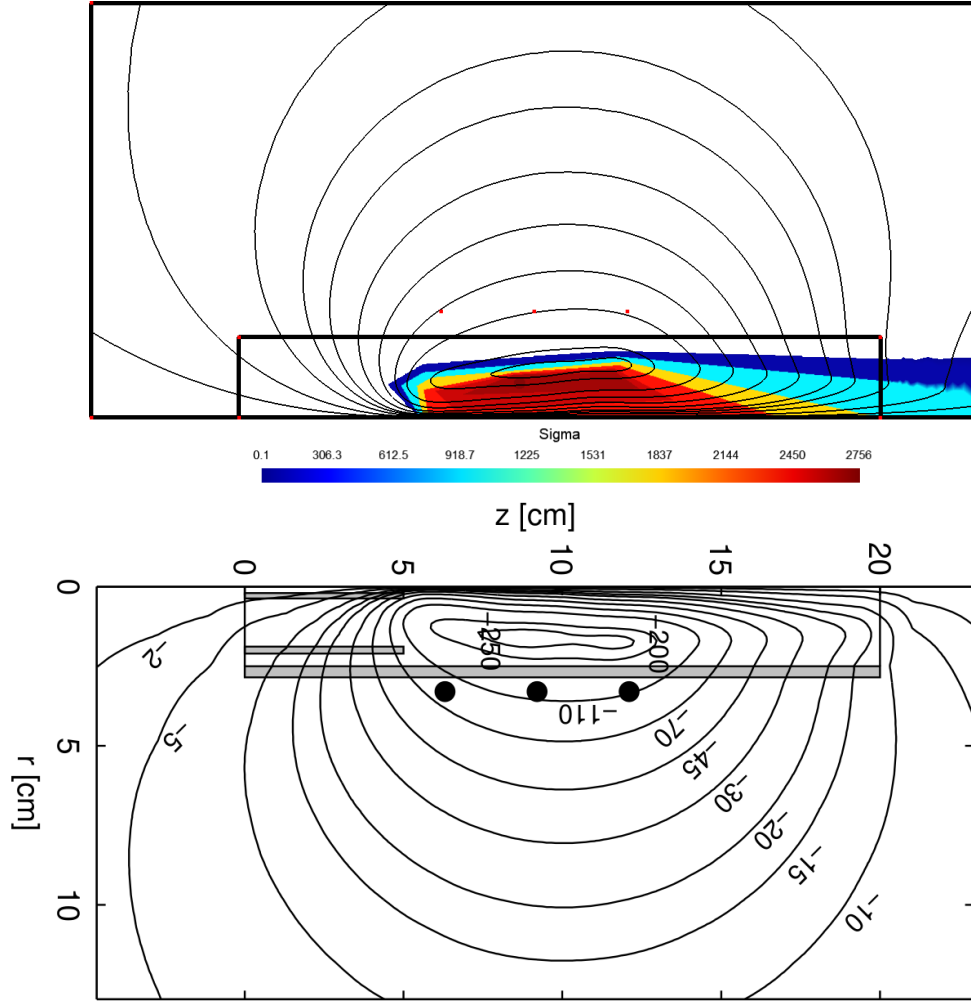


**Figure 3.14:** Iso-value lines of the real part of the total electric field. (top) Present results with distribution of the electrical conductivity and (bottom) results from Bernardi *et al.* [6].



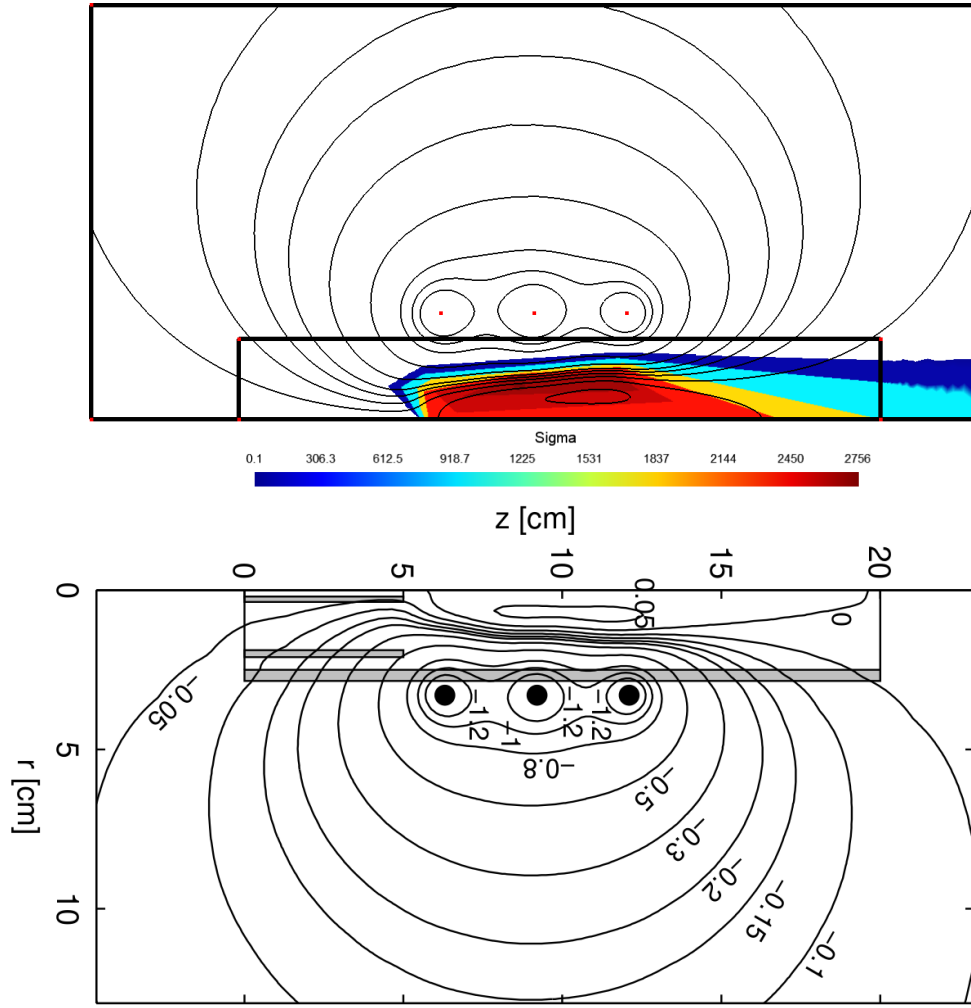


**Figure 3.15:** Iso-value lines of the imaginary part of the total electric field. (top) Present results with distribution of the electrical conductivity and (bottom) results from Bernardi *et al.* [6].

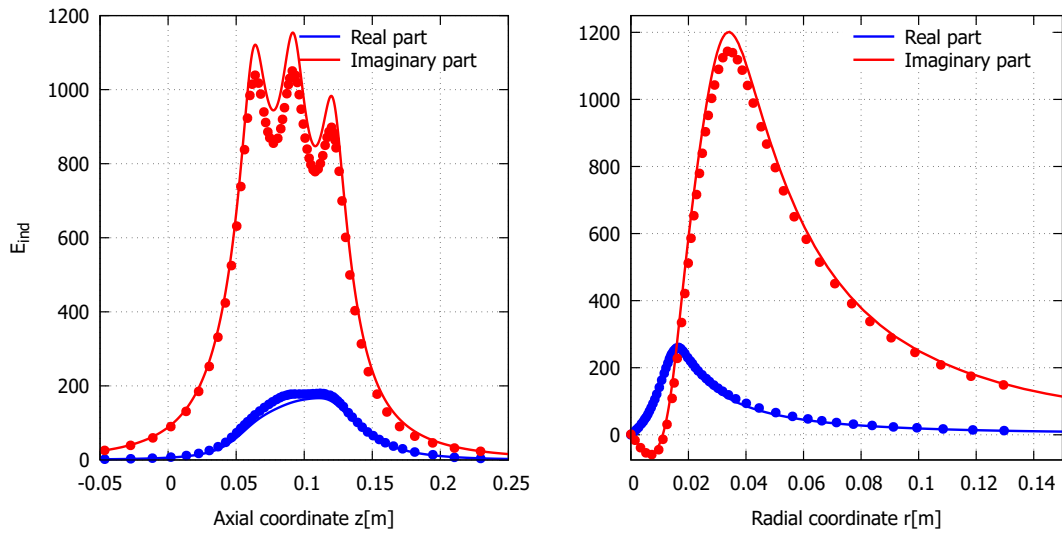


**Figure 3.16:** (left) Axial (on the wall) and (right) radial (at  $z = 0.102m$ ) cuts of the real and imaginary parts of the total electric field with numerical results from Bernardi *et al.* [6].

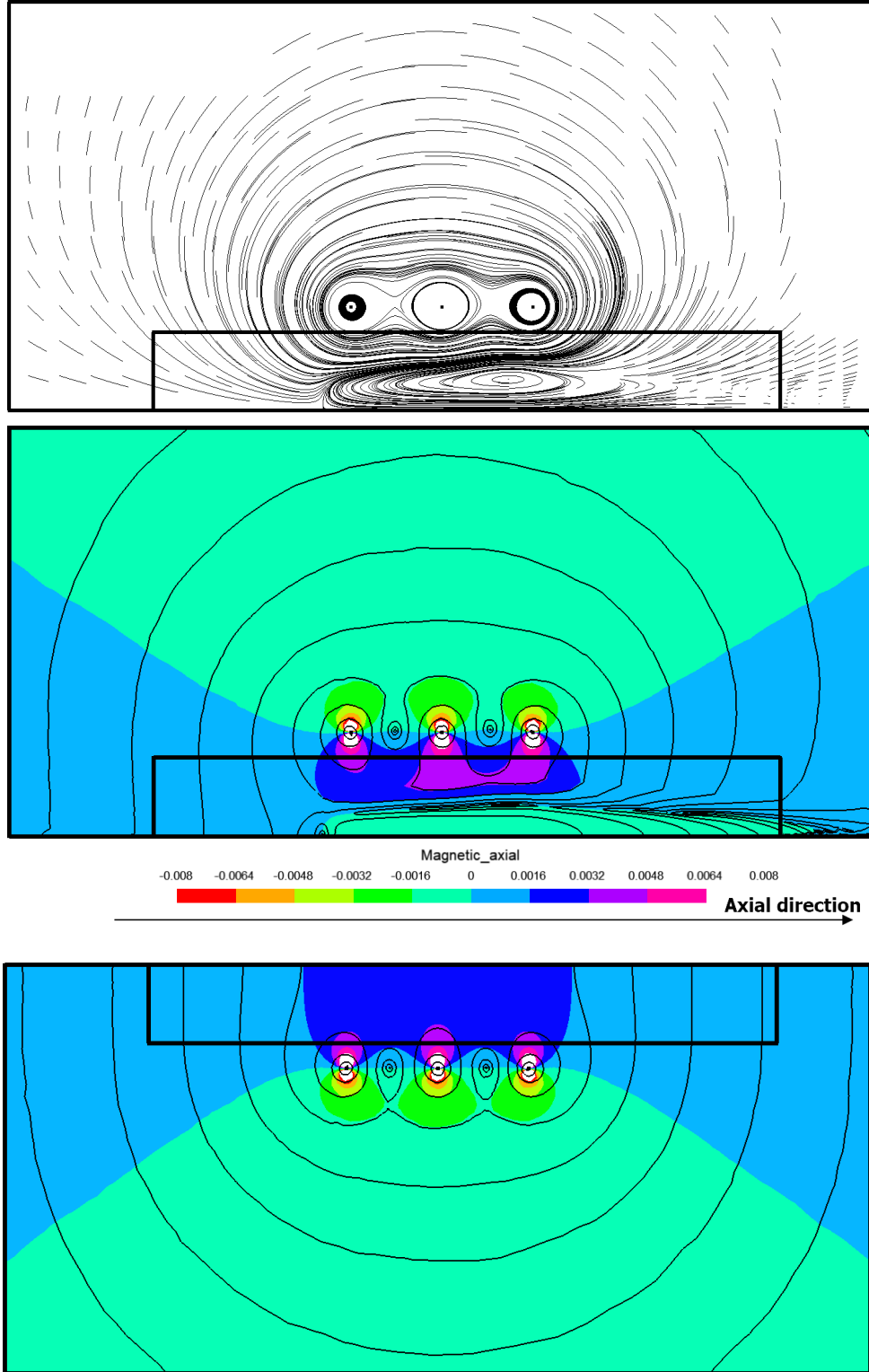


**Figure 3.17:** (top) Streamlines of the magnetic field. (middle and bottom) Iso-value lines of the norm of the magnetic field are superposed over the distribution of the axial component of the magnetic field. (middle) Present results with distribution of the electrical conductivity and (bottom) without plasma inside the torch.

# Bibliography

- [1] David vanden Abeele. *An efficient computational model for inductively coupled air plasma flows under thermal and chemical non-equilibrium - with application to atmospheric re-entry flow studies*. PhD thesis, Katholieke Universiteit Leuven, 2000.
- [2] J.W. McKelliget. A mathematical model of an inductive plasma torch. Technical Report 86-112.1, University of Lowell, College of Engineering, September 1986.
- [3] Silvânia Lopes. *Integrated CFD Model for Nanoparticle Production in Inductively Coupled Plasma Reactors: Implementation and Application*. PhD thesis, Université Libre de Bruxelles, 2016.
- [4] D. Bernardi, V. Colombo, G. G. M. Coppa, and A. D’Angola. Simulation of the ignition transient in RF inductively-coupled plasma torches. *The European Physical Journal D - Atomic, Molecular, Optical and Plasma Physics*, 14(3):337–348, 2001.
- [5] Yves Detandt. *Extension of Spectral/Finite Element solver for Large Eddy Simulation (SFE-LES) for axisymmetric bodies*. PhD thesis, Université Libre de Bruxelles, 2004.
- [6] D. Bernardi, V. Colombo, E. Ghedini, and A. Mentrelli. Comparison of different techniques for the FLUENT<sup>®</sup>-based treatment of the electromagnetic field in inductively coupled plasma torches. *The European Physical Journal D - Atomic, Molecular, Optical and Plasma Physics*, 27(1):55–72, 2003.
- [7] D. Bernardi, V. Colombo, E. Ghedini, and A. Mentrelli. Three-dimensional modeling of inductively coupled plasma torches. *Pure and Applied Chemistry*, 77(2):359–372, 2005.